THE JOURNAL OF PHYSICAL CHEMISTRY C
A JOURNAL OF THE AMERICAN CHEMICAL SOCIETY

pubs.acs.org/JPCC
Article

Surface Roughness Dependent Linear Electric Field Effects on the Exciton Absorption of Methylammonium Lead Triiodide Perovskite Films

Sudhakar Narra, Yu-Ling Chung, Shailesh Rana, Parameswaran Rajamanickam, Kamlesh Awasthi, Eric Wei-Guang Diau,* and Nobuhiro Ohta*

Cite This: J. Phys. Chem. C 2024, 128, 17134−17140
Read Online

ACCESS | Metrics & More | Article Recommendations | Supporting Information

ABSTRACT: Perovskite solar cells garnered commercial interest due to their device's impressive photon conversion efficiencies and improvements in long-term stabilities. The critical indicators of high-quality perovskite solar cells are often associated with morphological characteristics, such as grain size, compact packing, surface smoothness, and formation of suitable interfaces with charge transport layers. In the present study, the linear electroabsorption spectral signals emanating from the interface of methylammonium lead triiodide perovskite films grown on different electrodes and charge transport layers are shown to be sensitive to surface roughness. The polymeric hole transporting layers PEDOT:PSS on FTO/ITO substrates as underlayers were shown to produce smoother films with weaker linear electroabsorption signals compared with the tin oxide electron transporting layer on the FTO substrate as an underlayer, thereby highlighting the potential of linear electroabsorption spectroscopy to screen the quality of perovskite solar cells.

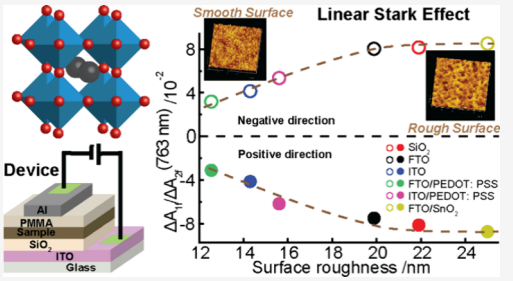

INTRODUCTION

Perovskite solar cells are marching forward with great strides due to the tremendous improvements in device architectures, efficiencies, and long-term stabilities compared with conventional solar cells. For example, the devices of single-junction perovskite solar cells reported an efficiency of 26.2%, while the silicon−perovskite tandem solar cell displayed an efficiency of 33.9%.[1−5] Further, the active areas of perovskite solar cells increased from millimeters to centimeters, and their device performance stabilities crossed several 1000 h, which has drawn commercial interest recently.[2,6−10] However, device performance degradation due to ion migration and deteriorating film quality due to aging or decomposition are still critical issues that must be overcome to match the stabilities of perovskite solar cell technologies on par with crystalline silicon solar cells.[11−15]

Interestingly, the performance and stabilities go hand in hand for perovskite solar cells. For example, E-beam inspections of highly functional and stable perovskite solar cells display compact packing, moderate crystallite sizes, and smooth surfaces/interfaces.[16−21] By taking the cues from successful device architectures, several interesting structural engineering techniques have been introduced to enhance the longevity and performance of the devices. For example, molecular additives were used to passivate the defects; the bifunctional self-assembled monolayers were introduced between the electrodes and the perovskite films to pacify interfacial defects and improve the charge transport, and/or the surface passivation was done with a two-dimensional perovskite, polymeric materials, or small molecules to protect the top surface from degradation and nullify the surface defects.[2,4,6,22−28] Therefore, it is imperative to develop a molecular understanding of the effects of interfacial and morphological characteristics of the absorbing layers on the electronic properties of perovskite solar cell devices.

Electroabsorption (E-A) spectroscopy is a powerful tool in providing a molecular level understanding of the excitons produced in the bulk and interfaces with electrodes or charge transporting materials. E-A spectra obtained by synchronizing the field-induced change in transmitted light intensity at the second harmonic of the modulation frequency have been used to determine the exciton binding energies and effective masses of carriers of perovskite nanocrystalline films.[29−36] The effects of irradiation light intensity and the modulation frequency dependence of the applied external electric field on the ion migration kinetics have been studied using second-harmonic E-A spectroscopy.[31] Similarly, E-A spectra obtained by synchronizing the field-induced change in transmitted light

Received: July 11, 2024
Revised: September 6, 2024
Accepted: September 14, 2024
Published: September 26, 2024

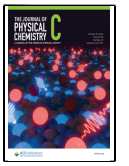

https://doi.org/10.1021/acs.jpcc.4c04645
J. Phys. Chem. C 2024, 128, 17134−17140

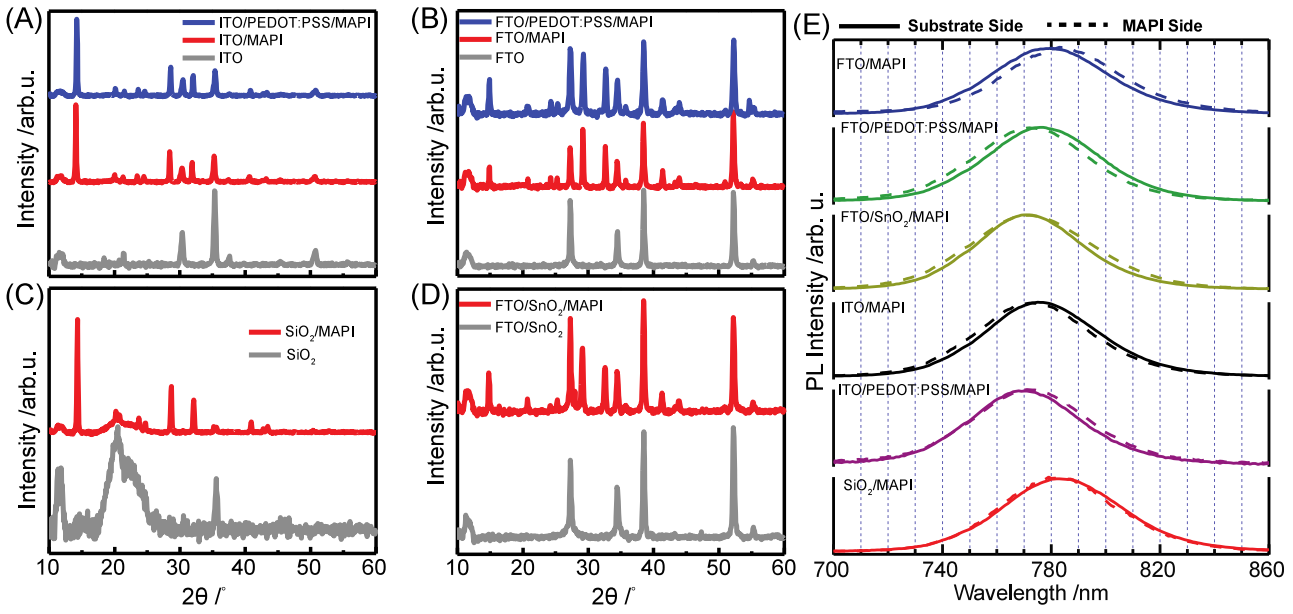

Figure 1. (A–D) XRD patterns of MAPI films grown on various underlayers. (E) Surface-sensitive PL spectra of MAPI films grown on multiple underlayers observed for its substrate side and MAPI side with an excitation wavelength of 450 nm.

intensity at the first harmonic of the modulation frequency have been used to discuss the electronic structure of molecules at the interfaces for orderly arranged systems, quantum wells, and perovskite films.[37−41] Usually, the first harmonic E-A spectra produce first-derivative line shapes due to the linear Stark effect. However, the first harmonic E-A spectra of methylammonium lead triiodide (MAPI) perovskite films were found to show second derivative-like shapes similar to those obtained at the second harmonic of the modulation frequency, which was assigned to the coexistence of both spectral broadening and narrowing processes.[37] Recently, it was proposed that the second-derivative-like shape of the first harmonic E-A spectra arose due to the differences in electronic structures of MAPI films at the top and bottom interfaces, which undergo red and blue Stark shifts upon application of the external field.[33] Herein, we show that the magnitude of the first harmonic E-A signal is very sensitive to the underlayer on which the perovskite film is grown. The film roughness of perovskites is highly correlated to the functioning of its devices. Similar to the device performance, the first harmonic E-A signals are also shown to be associated with the roughness of the perovskite films. Then, first-harmonic E-A spectroscopy is proposed as an excellent option to examine the interface quality of perovskite solar cells for their functionality and longevity.

EXPERIMENTAL METHODS

Indium tin oxide (ITO) and fluorine tin oxide (FTO) substrates of size 3 cm × 2 cm were taken, and half of the substrate was etched using zinc powder and 4 M hydrochloric acid. The other half of the substrate was protected by masking with Scotch brand tape during etching. The etched substrates were thoroughly cleaned with water and detergent, followed by ultrasonication twice in a solution of 1:1:1 ratio of water:-acetone:isopropanol mixture. The ultrasonicated substrates were rinsed with DI water, followed by pure acetone, and then dried in the laboratory oven for about 3 h to ensure enough drying of the substrates. The dried substrates were ozonized for 30 min before spin-coating to improve the surface wettability.

Poly(3,4-ethylenedioxythiophene)−poly(styrenesulfonate) (PEDOT:PSS) and tin oxide (SnO_2) nanoparticle suspension in water (H_2O) were taken in sample vials, stirred, and sonicated for 30 min to ensure no aggregation. Further, the dispersions were filtered using 0.45 μm nylon filter to separate larger particles. Later, the suspensions were spread over the substrates and spin-coated using a spin-coating machine set to 5000 rpm for 50 s. The spin-coated films were annealed at 150 °C for 10 and 30 min for PEDOT:PSS and SnO_2 samples.

Later, MAPI films were spin-cast onto the substrates inside a glovebox kept under the steady flow of dry nitrogen. MAPI films were prepared using a mixture of lead iodide (PbI_2) and methylammonium iodide (MAI) in a 1:1 ratio dissolved in dimethylformamide solvent. The precursor solution was stirred for 12 h at 70 °C, filtered, and cooled to room temperature before spin-coating. The MAPI films were spin-cast from the precursor solutions using the antisolvent spin-coating method, where precursor solution was loaded onto the substrates and the rotor of the spin coater was spun at 5000 rpm for 50 s. At 5 s after the initiation of the rotation, chlorobenzene was dropped onto the substrate at normal incidence to retard the nucleation and improve the quality of the fabricated films. The spin-coated samples were annealed at 100 °C for 10 min. During the annealing process, the films turn from transparent to dark brown color, ensuring the formation of perovskite crystals.

An insulating poly(methyl methacrylate) (PMMA) film was spun on top of MAPI to prevent it from degradation due to moisture and oxygen. 45 mg of purified PMMA was dissolved in 1 mL of toluene and stirred to obtain a clear precursor solution suitable for spin-coating. PMMA precursor solution was loaded onto the MAPI film and spin-coated at 5000 rpm for 50 s. The 18 nm thick semitransparent aluminum electrodes were deposited on top of the PMMA film using the vacuum thermal deposition method. The films deposited between the two electrodes, i.e., the conducting layer and aluminum electrode, serve as active layers for applying the

https://doi.org/10.1021/acs.jpcc.4c04645
J. Phys. Chem. C 2024, 128, 17134−17140

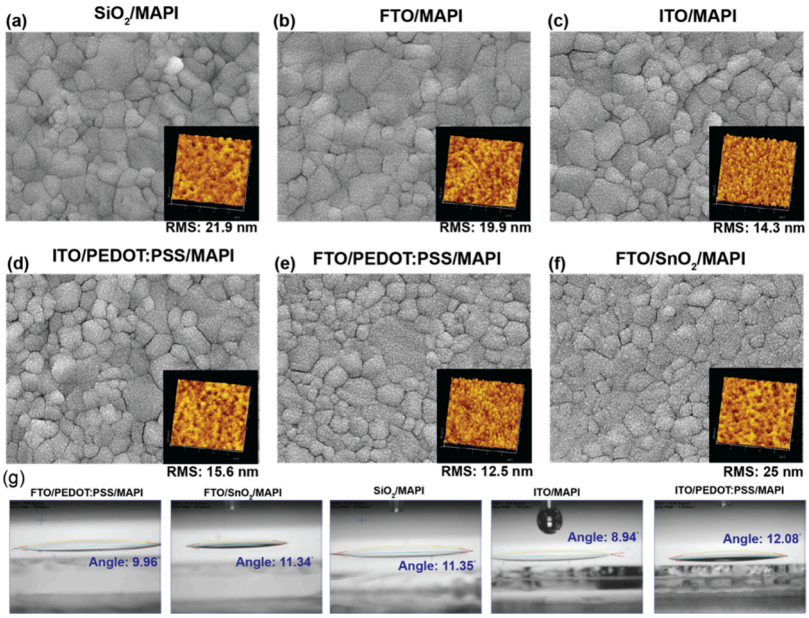

Figure 2. Scanning electron micrograph (SEM) images of MAPI perovskite grown on (a) SiO_2, (b) FTO, (c) ITO, (d) ITO/PEDOT:PSS, (e) FTO/PEDOT:PSS, and (f) FTO/SnO_2 underlayers. The insets on the SEM images are the atomic force micrographs displaying the surface roughness of the corresponding films. (g) Contact angles of precursor solutions on various layers as indicated.

electric field. The thickness of the active layers was determined by using a surface profiler (Dektak 150, Veeco).

The UV−vis absorption spectra of the perovskite samples were measured using a JASCO spectrometer. The PL spectra of perovskite samples were measured using a laboratory-built PL spectroscopic system reported elsewhere.[46] A 450 nm CW diode laser was used as an excitation light source, and the emission spectrum was measured by scanning the monochromator's grating and coupling the output to a silicon photodiode and a digital multimeter. The excitation light was blocked at the entrance of the monochromator using a 500 nm long pass filter. The X-ray diffraction patterns were recorded from a Bruker D8 Advance diffractometer equipped with monochromatic Cu Kα radiation (λ = 1.5406 Å) operating at 40 kV and 40 mA. The samples were probed from $2\theta = 10°$ to 60° at an increment of 0.0745°. Background correction is performed on the acquired XRD patterns. For the contact angle measurement, about 10 μL of the perovskite precursor solution was carefully dropped on the substrate of interest and placed on top of a glass plate holder. The droplet−substrate interaction was viewed, and the corresponding image was captured through a CCD camera, followed by the direct contact angle calculation using FTA32 software. The scanning electron microscopic images were measured using a Hitachi SU8010, and atomic force micrographs were obtained using a SEIKO SPA-300HV. As described elsewhere, the field-induced change in the absorption spectra of MAPI samples was obtained using a laboratory-built electroabsorption spectroscopic system.[29−34,37,47] A sinusoidal wave of frequency 1 kHz and electric field strengths of 0.05−0.3 MVcm^{-1} were applied to samples to measure the E-A spectra with respect to the first harmonic and second harmonic of the applied field.

RESULTS AND DISCUSSION

MAPI perovskite films were grown on different underlayers, namely, SiO_2, FTO, ITO, ITO/PEDOT:PSS, FTO/PEDOT:PSS, and FTO/SnO_2 underlayers. Here, SiO_2 is an insulator commonly used in E-A spectroscopy, whereas FTO and ITO are electrodes used in n−i−p and p−i−n architecture of solar cells, and PEDOT:PSS and SnO_2 are hole and electron transporting materials, respectively. XRD patterns of the fabricated MAPI films on various underlayers are shown in Figure 1A−D. The XRD patterns broadly resemble the well-known room temperature tetragonal phase[42] of MAPI; however, the peak intensities and positions show sensitivity to the underlayer used to grow the films. For example, the 14° peak displayed a weaker intensity for MAPI films grown on FTO than on ITO or SiO_2 underlayers. The absorption spectra of MAPI films grown on various underlayers are shown in Figure S1. The absorption spectra show band edges due to the excitonic bands with band tails and slight variations in the absorbance values. The variations in the absorbance values of the films could be due to differences in the thicknesses of the films grown on different underlayers. The effects of the substrate on the electronic band structures were studied using surface-sensitive photoluminescence (PL) spectroscopy, as shown in Figure 1E. The PL spectra of MAPI films show emission bands from the band edge states in the region between 770 and 780 nm as listed in Table S1. The peak position and bandwidth of the PL spectra of MAPI films are sensitive both to the growth substrate and to the measurement direction (e.g., measurements from the substrate side vs opposite film side), suggesting that both band bending and perovskite film quality such as morphology or surface roughness depends on the growth substrate and the interface between MAPI and substrate.

Scanning electron microscopy (SEM) and atomic force microscopy (AFM) images were taken to probe the effect of the underlayer on the surface morphology and roughness, as shown in Figure 2. SEM images show that MAPI films fabricated on different underlayers produced good-quality films without any pinholes. The underlayers affected the grain size distributions and surface roughness of the films, as shown by the SEM and AFM images. ITO electrodes produced smoother

https://doi.org/10.1021/acs.jpcc.4c04645
J. Phys. Chem. C 2024, 128, 17134−17140

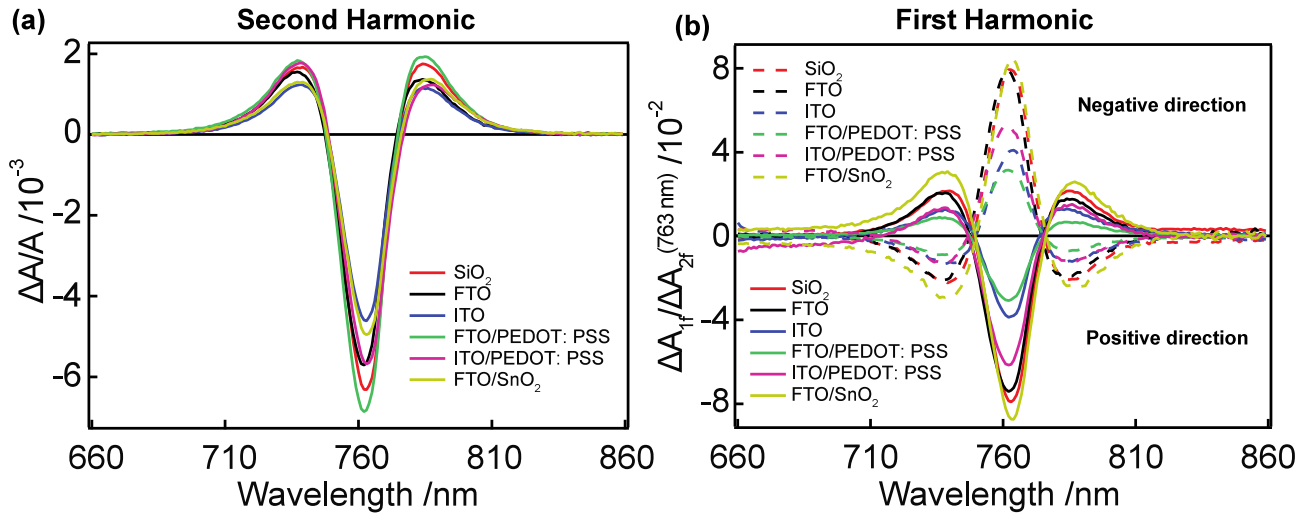

Figure 3. E-A spectra of MAPI films grown on various underlayers as a function of (a) second harmonic (EA_{2f}) and (b) first harmonic (EA_{1f}) of the applied ac sine wave modulation frequency. The modulation frequency was set to 1 kHz, and the field strength was set to 0.3 MV cm^{-1}.

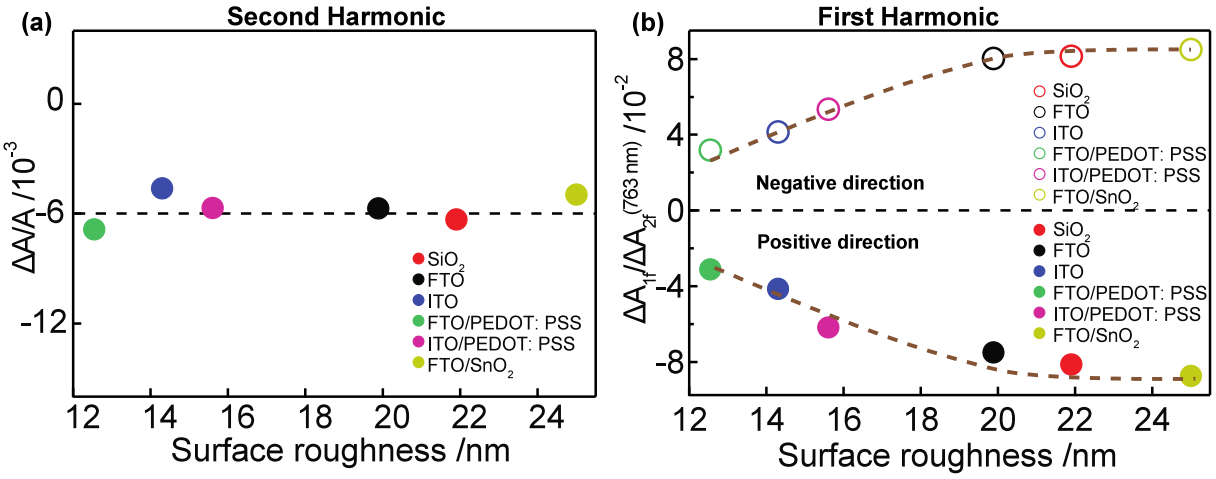

Figure 4. Effects of surface roughness on EA signal magnitudes were monitored at (a) the second harmonic and (b) the first harmonic relative to the applied frequency. Broken lines are guides for the eye.

films than did the FTO and SiO_2 insulator underlayers. Introducing the PEDOT:PSS polymeric hole transport layer decreased the surface roughness of MAPI films produced on FTO plates, whereas the SnO_2 metal oxide electron transporting layer increased the surface roughness of the MAPI film. All in all, FTO/PEDOT:PSS produced a smoother film with a surface roughness of 12.5 nm, and FTO/SnO_2 produced a rough film with a surface roughness of 25 nm. The observed variations in the surface roughness of MAPI films can be ascribed to changes in the nucleation rate caused by the change in the surface wettability of the underlayers. Contact angle measurements shown in Figure 2g show the underlayer dependent variations in the surface wettability with variations of 3°. The contact angles of precursor solutions on ITO and FTO/PEDOT:PSS surfaces were shown to be ∼9° and 10°, respectively, which produced smoother MAPI film surfaces with roughness of 14.3 and 15.6 nm, respectively.

In the present study, E-A spectra of MAPI film fabricated on different substrates were measured at the second harmonic and first harmonic of the modulation frequency of the applied electric field, as shown in Figure 3. The second harmonic E-A (EA_{2f}) spectra show characteristic second-derivative-like band shapes under the presence of the applied electric field. The magnitudes of EA_{2f} signals grow linearly (refer to Figure S2) to the square of the applied electric field. The second-derivative-like shape of the EA_{2f} excitonic absorption band results from the broadening of exciton absorption bands upon application of the external electric field. The broadening of excitonic bands was assigned to a change in the sample's electric dipole moment ($\Delta\mu$) following absorption, associated with the applied electric field.[29,31,33,34] The observed EA_{2f} spectra were scaled to the absorbance values of their excitonic absorption bands to nullify the effects of thickness on the magnitude of the observed changes. The EA_{2f} spectra show slight variation in the signal intensities based on the underlayer used for film growth, but this purely comes from the sample condition, which can be regarded as an experimental error.

As shown in Figure 3, the first harmonic E-A (EA_{1f}) spectra also show a second-derivative-like band shape similar to the EA_{2f} spectra, but a switching behavior with respect to the polarity of the applied field was observed, in contrast to the EA_{2f} spectra. The EA_{1f} spectral band magnitudes grow linearly with respect to the applied field (refer to Figure S3), confirming the origin of the observed spectra. Note that the

https://doi.org/10.1021/acs.jpcc.4c04645
J. Phys. Chem. C 2024, 128, 17134−17140

EA_{2f} spectral signal grows linearly to the square of the applied electric field, as mentioned above. The observed second-derivative-like shape of the EA_{1f} spectra and polarity dependence are consistent with the earlier reports.[33,37] The EA_{1f} spectra often produce first-derivative shapes in highly oriented samples and no signals in randomly oriented samples. The first-derivative shape of the EA_{1f} spectra in the oriented samples is due to the shift of excitonic absorption bands caused by $\Delta\mu$ following absorption in the presence of the applied electric field, whereas in randomly oriented samples these spectral shifts cancel out on an ensemble average, leading to no signals. Contrary to expectations, EA_{1f} spectra of MAPI samples show second-derivative-like shapes. Recently, it was reported that the observed second-derivative-like shapes of the EA_{1f} spectra originate from different magnitudes of the spectral shifts arising from the top and bottom interfaces of MAPI films.[33] Similar to the EA_{2f} spectra, EA_{1f} spectra were also scaled to nullify the effects of the second harmonic field on the first harmonic signals in Figure 3.

The magnitudes of EA_{2f} and EA_{1f} signals at the minimum peak of the exciton band were plotted against sample roughness as shown in Figure 4. The EA_{2f} signals show a random distribution within experimental uncertainties, whereas EA_{1f} signals show an excellent correlation to the surface roughness, i.e., with a plateauing effect for roughness over 20 nm. FTO/PEDOT:PSS/MAPI film with a surface roughness of 12.5 nm showed a weaker first harmonic E-A band intensity, whereas FTO/SnO_2/MAPI with a surface roughness of 25 nm showed a stronger first harmonic band intensity. The underlying physics behind the observed correlation between the film surfaces and the EA_{1f} signals might have multiple origins , such as the accumulation of space charges at the opposite electrodes due to photoexcitation, ion migration, optical interference, interface defects, etc. However, effects such as optical interference and ion migration can be ignored as the former is more sensitive to reflection mode measurements than the transmission mode measurements, and likewise, the latter is manifested at low frequencies and high photon fluxes. The EA experiments were conducted at high frequencies and low photon fluxes where ion migration is minimal. Therefore, the observed EA_{1f} signals might be a result of asymmetric electric fields at the interfaces due to dangling bonds or accumulated space charges where the former is more likely than the latter as the photon fluxes are small but cannot be ruled out. Similarly, differences in the orientations of grains or grain sizes at the interfaces may also lead to asymmetric electric fields and to EA_{1f} signals; however, they are not possible to quantify, as the back interfaces are always buried. Further, the grain sizes and surface morphologies shown from the SEM images in Figure 2 do not offer quantifiable changes that can be correlated to EA_{1f} signals, but the surface roughness parameter evaluated from AFM that correlates quite well to the EA_{1f} signals is usually a manifestation of various underlying physical phenomena mentioned above.

Despite the complex physical processes, the observed correlation of EA_{1f} signals with surface roughness has practical implications. For example, the performance of MAPI solar cell devices and their hysteresis effects were often shown to be sensitive to film surface roughness. MAPI films with smoother morphologies displayed higher efficiencies, minimal hysteresis, and long stability.[17,18,20,21,43−45] SEM micrographs can be used to assess the quality of films; however, they need special sampling procedures, and films cannot be used after the measurements. However, EA measurements can be performed on the working devices without impacting their performances. Therefore, the correlation of EA_{1f} signal magnitudes with surface roughness is quite interesting as they serve as visual guides to connect the molecular properties with the device's electrical properties. It is worth mentioning that simple electric field effects on steady-state absorption techniques have the potential to be used as a valuable tool to screen fabricated perovskite films (developed using various methods on a variety of underlayers) for their quality and to correlate device performances with respect to standard devices.

CONCLUSIONS

In summary, MAPI films on different substrates grown under identical conditions show variations in grain sizes and roughness. ITO substrate was shown to produce smoother films when compared with FTO or SiO_2 substrates as underlayers. Polymeric PEDOT:PSS hole transporting layers deposited on FTO/ITO substrates were shown to produce smoother films when compared with electron transporting layers deposited on FTO substrates. First-harmonic E-A spectra were shown to have a clear correlation with the surface roughness, whereas second-harmonic E-A spectra were shown to be insensitive to the surface morphological conditions within the experimental uncertainties. The sensitivity of the first-harmonic E-A signal to surface roughness might serve as an excellent indicator to characterize the interfaces of perovskite solar cells to predict their quality for long-term operation.

ASSOCIATED CONTENT

Supporting Information

The Supporting Information is available free of charge at https://pubs.acs.org/doi/10.1021/acs.jpcc.4c04645.

UV−vis absorption spectra of MAPbI films grown on various underlayers; field strength dependence of the second harmonic and the first harmonic signals for MAPbI films grown on different underlayers; emission band peak position and bandwidths of MAPI films grown on various underlayers (PDF)

AUTHOR INFORMATION

Corresponding Authors

Eric Wei-Guang Diau − *Department of Applied Chemistry and Institute of Molecular Science and Center for Emergent Functional Matter Science, National Yang Ming Chiao Tung University, Hsinchu 30010, Taiwan;* orcid.org/0000-0001-6113-5679; Email: diau@nycu.edu.tw

Nobuhiro Ohta − *Department of Applied Chemistry and Institute of Molecular Science and Center for Emergent Functional Matter Science, National Yang Ming Chiao Tung University, Hsinchu 30010, Taiwan;* orcid.org/0000-0003-4255-6448; Email: nohta@nycu.edu.tw

Authors

Sudhakar Narra − *Department of Applied Chemistry and Institute of Molecular Science and Center for Emergent Functional Matter Science, National Yang Ming Chiao Tung University, Hsinchu 30010, Taiwan;* orcid.org/0000-0003-4893-9204

Yu-Ling Chung − *Department of Applied Chemistry and Institute of Molecular Science, National Yang Ming Chiao Tung University, Hsinchu 30010, Taiwan*

Shailesh Rana − *Department of Applied Chemistry and Institute of Molecular Science, National Yang Ming Chiao Tung University, Hsinchu 30010, Taiwan;* orcid.org/0000-0002-4349-101X

Parameswaran Rajamanickam − *Department of Material Science and Engineering, National Yang Ming Chiao Tung University, Hsinchu 30010, Taiwan;* orcid.org/0000-0001-9377-2963

Kamlesh Awasthi − *Department of Applied Chemistry and Institute of Molecular Science and Center for Emergent Functional Matter Science, National Yang Ming Chiao Tung University, Hsinchu 30010, Taiwan;* orcid.org/0000-0001-7852-059X

Complete contact information is available at: https://pubs.acs.org/10.1021/acs.jpcc.4c04645

Notes

The authors declare no competing financial interest.

■ ACKNOWLEDGMENTS

This work was supported by the National Science and Technology Council, Taiwan (NSTC 111-2113-M-A49-015). This work was also supported financially by The Center for Emergent Functional Matter Science of National Yang Ming Chiao Tung University from The Featured Areas Research Center Program within the framework of the Higher Education Sprout Project by the Ministry of Education (MOE) in Taiwan.

■ REFERENCES

(1) Kojima, A.; Teshima, K.; Shirai, Y.; Miyasaka, T. Organometal Halide Perovskites as Visible-Light Sensitizers for Photovoltaic Cells. *J. Am. Chem. Soc.* **2009**, *131* (17), 6050−6051.

(2) Ding, B.; Ding, Y.; Peng, J.; Romano-deGea, J.; Frederiksen, L. E. K.; Kanda, H.; Syzgantseva, O. A.; Syzgantseva, M. A.; Audinot, J.-N.; Bour, J.; Zhang, S.; Wirtz, T.; Fei, Z.; Dörflinger, P.; Shibayama, N.; Niu, Y.; Hu, S.; Zhang, S.; Tirani, F. F.; Liu, Y.; Yang, G.-J.; Brooks, K.; Hu, L.; Kinge, S.; Dyakonov, V.; Zhang, X.; Dai, S.; Dyson, P. J.; Nazeeruddin, M. K. Dopant-Additive Synergism Enhances Perovskite Solar Modules. *Nature* **2024**, *628*, 299−305.

(3) Aydin, E.; Allen, T. G.; De Bastiani, M.; Razzaq, A.; Xu, L.; Ugur, E.; Liu, J.; De Wolf, S. Pathways toward Commercial Perovskite/Silicon Tandem Photovoltaics. *Science* **2024**, *383* (6679), No. eadh3849.

(4) Pappenberger, R.; Diercks, A.; Petry, J.; Moghadamzadeh, S.; Fassl, P.; Paetzold, U. W. Bandgap Engineering of Two-Step Processed Perovskite Top Cells for Perovskite-Based Tandem Photovoltaics. *Adv. Funct. Mater.* **2024**, *34* (9), No. 2311424.

(5) De Bastiani, M.; Subbiah, A. S.; Babics, M.; Ugur, E.; Xu, L.; Liu, J.; Allen, T. G.; Aydin, E.; De Wolf, S. Bifacial Perovskite/Silicon Tandem Solar Cells. *Joule* **2022**, *6* (7), 1431−1445.

(6) Park, S. M.; Wei, M.; Xu, J.; Atapattu, H. R.; Eickemeyer, F. T.; Darabi, K.; Grater, L.; Yang, Y.; Liu, C.; Teale, S.; Chen, B.; Chen, H.; Wang, T.; Zeng, L.; Maxwell, A.; Wang, Z.; Rao, K. R.; Cai, Z.; Zakeeruddin, S. M.; Pham, J. T.; Risko, C. M.; Amassian, A.; Kanatzidis, M. G.; Graham, K. R.; Grätzel, M.; Sargent, E. H. Engineering Ligand Reactivity Enables High-Temperature Operation of Stable Perovskite Solar Cells. *Science* **2023**, *381* (6654), 209−215.

(7) Habisreutinger, S. N.; Reese, M. O. Building Perovskite Solar Cells That Last. *Science* **2022**, *377* (6603), 265−266.

(8) Rajamanickam, P.; Narra, S.; Seetharaman, A.; Diau, E. W.-G. Highly Efficient HTM-Free Tin Perovskite Solar Cells with Outstanding Stability Exceeding 10000 h. *ACS Appl. Mater. Interfaces* **2023**, *15* (34), 40700−40708.

(9) Zhu, H.; Teale, S.; Lintangpradipto, M. N.; Mahesh, S.; Chen, B.; McGehee, M. D.; Sargent, E. H.; Bakr, O. M. Long-Term Operating Stability in Perovskite Photovoltaics. *Nat. Rev. Mater.* **2023**, *8* (9), 569−586.

(10) Duan, L.; Walter, D.; Chang, N.; Bullock, J.; Kang, D.; Phang, S. P.; Weber, K.; White, T.; Macdonald, D.; Catchpole, K.; Shen, H. Stability Challenges for the Commercialization of Perovskite−Silicon Tandem Solar Cells. *Nat. Rev. Mater.* **2023**, *8* (4), 261−281.

(11) Pockett, A.; Spence, M.; Thomas, S. K.; Raptis, D.; Watson, T.; Carnie, M. J. Beyond the First Quadrant: Origin of the High Frequency Intensity-Modulated Photocurrent/Photovoltage Spectroscopy Response of Perovskite Solar Cells. *Sol. RRL* **2021**, *5* (5), No. 2100159.

(12) Gets, D. S.; Verkhogliadov, G. A.; Danilovskiy, E. Y.; Baranov, A. I.; Makarov, S. V.; Zakhidov, A. A. Dipolar Cation Accumulation at the Interfaces of Perovskite Light-Emitting Solar Cells. *J. Mater. Chem. C* **2020**, *8* (47), 16992−16999.

(13) Bae, S.; Kim, S.; Lee, S.-W.; Cho, K. J.; Park, S.; Lee, S.; Kang, Y.; Lee, H.-S.; Kim, D. Electric-Field-Induced Degradation of Methylammonium Lead Iodide Perovskite Solar Cells. *J. Phys. Chem. Lett.* **2016**, *7* (16), 3091−3096.

(14) Aranda, C. A.; Alvarez, A. O.; Chivrony, V. S.; Das, C.; Rai, M.; Saliba, M. Overcoming Ionic Migration in Perovskite Solar Cells through Alkali Metals. *Joule* **2024**, *8* (1), 241−254.

(15) Yantara, N.; Mathews, N. Toolsets for Assessing Ionic Migration in Halide Perovskites. *Joule* **2024**, *8* (5), 1239−1273.

(16) Nukunudompanich, M.; Budiutama, G.; Suzuki, K.; Hasegawa, K.; Ihara, M. Dominant Effect of the Grain Size of the MAPbI 3 Perovskite Controlled by the Surface Roughness of TiO_2 on the Performance of Perovskite Solar Cells. *CrystEngComm* **2020**, *22* (16), 2718−2727.

(17) Lee, H. B.; Jeon, M.; Kumar, N.; Tyagi, B.; Kang, J. Boosting the Efficiency of SnO_2-Triple Cation Perovskite System Beyond 20% Using Nonhalogenated Antisolvent. *Adv. Funct. Mater.* **2019**, *29* (32), No. 1903213.

(18) Wu, W.-Q.; Chen, D.; Huang, F.; Cheng, Y.-B.; Caruso, R. A. Optimizing Semiconductor Thin Films with Smooth Surfaces and Well-Interconnected Networks for High-Performance Perovskite Solar Cells. *J. Mater. Chem. A* **2016**, *4* (32), 12463−12470.

(19) Shi, Y.; Zheng, Y.; Xiao, X.; Wang, P.; Zhang, G.; Li, Q.; Zhang, G.; Shao, Y. Vertical Grain-Shape Engineering for High-Efficiency and Stable Perovskite Solar Cells. *Cell Rep. Phys. Sci.* **2023**, *4* (11), No. 101649.

(20) Chen, Q.; Zhou, H.; Hong, Z.; Luo, S.; Duan, H.-S.; Wang, H.-H.; Liu, Y.; Li, G.; Yang, Y. Planar Heterojunction Perovskite Solar Cells via Vapor-Assisted Solution Process. *J. Am. Chem. Soc.* **2014**, *136* (2), 622−625.

(21) Holzhey, P.; Prettl, M.; Collavini, S.; Mortan, C.; Saliba, M. Understanding the Impact of Surface Roughness: Changing from FTO to ITO to PEN/ITO for Flexible Perovskite Solar Cells. *Sci. Rep.* **2023**, *13* (1), 6375.

(22) Liu, Z.; Qiu, L.; Ono, L. K.; He, S.; Hu, Z.; Jiang, M.; Tong, G.; Wu, Z.; Jiang, Y.; Son, D.-Y.; Dang, Y.; Kazaoui, S.; Qi, Y. A Holistic Approach to Interface Stabilization for Efficient Perovskite Solar Modules with over 2,000-h Operational Stability. *Nat. Energy* **2020**, *5* (8), 596−604.

(23) Noel, N. K.; Habisreutinger, S. N.; Wenger, B.; Klug, M. T.; Hörantner, M. T.; Johnston, M. B.; Nicholas, R. J.; Moore, D. T.; Snaith, H. J. A Low Viscosity, Low Boiling Point, Clean Solvent System for the Rapid Crystallisation of Highly Specular Perovskite Films. *Energy Environ. Sci.* **2017**, *10* (1), 145−152.

(24) Das, C.; Kot, M.; Hellmann, T.; Wittich, C.; Mankel, E.; Zimmermann, I.; Schmeisser, D.; Nazeeruddin, M. K.; Jaegermann, W. Atomic Layer-Deposited Aluminum Oxide Hinders Iodide Migration and Stabilizes Perovskite Solar Cells. *Cell Rep. Phys. Sci.* **2020**, *1* (7), No. 100112.

(25) Yang, C.; Yin, J.; Li, H.; Almasabi, K.; Gutiérrez-Arzaluz, L.; Gereige, I.; Brédas, J.-L.; Bakr, O. M.; Mohammed, O. F. Engineering Surface Orientations for Efficient and Stable Hybrid Perovskite Single-Crystal Solar Cells. *ACS Energy Lett.* **2022**, *7* (4), 1544−1552.
(26) Seetharaman, A.; Narra, S.; Rajamanickam, P.; Putikam, R.; Lin, M.-C.; Diau, E. W.-G. Diffusion of Bulky Organic Cations in the 3D/2D Heterostructures to Form Interfacial Quasi-2D (N2) Phase for Tin Perovskite Solar Cells. *J. Mater. Chem. A* **2023**, *11* (39), 21089−21098.
(27) Jokar, E.; Cheng, P.-Y.; Lin, C.-Y.; Narra, S.; Shahbazi, S.; Diau, E. W.-G. Enhanced Performance and Stability of 3D/2D Tin Perovskite Solar Cells Fabricated with a Sequential Solution Deposition. *ACS Energy Lett.* **2021**, *6* (2), 485−492.
(28) Grancini, G.; Roldan-Carmona, C.; Zimmermann, I.; Mosconi, E.; Lee, X.; Martineau, D.; Narbey, S.; Oswald, F.; De Angelis, F.; Graetzel, M.; Nazeeruddin, M. K. One-Year Stable Perovskite Solar Cells by 2D/3D Interface Engineering. *Nat. Commun.* **2017**, *8*, 15684.
(29) Awasthi, K.; Du, K.-B.; Wang, C.-Y.; Tsai, C.-L.; Hamada, M.; Narra, S.; Diau, E. W.-G.; Ohta, N. Electroabsorption Studies of Multicolored Lead Halide Perovskite Nanocrystalline Solid Films. *ACS Photonics* **2018**, *5* (6), 2408−2417.
(30) Kattoor, V.; Awasthi, K.; Jokar, E.; Diau, E. W.-G.; Ohta, N. Enhanced Dissociation of Hot Excitons with an Applied Electric Field under Low-Power Photoexcitation in Two-Dimensional Perovskite Quantum Wells. *J. Phys. Chem. Lett.* **2019**, *10* (16), 4752−4757.
(31) Rana, S.; Awasthi, K.; Diau, E. W.-G.; Ohta, N. Illumination Power-Dependent Electroabsorption of Excitons in a $CH_3NH_3PbI_3$ Perovskite Film. *J. Phys. Chem. C* **2021**, *125* (50), 27631−27637.
(32) Kattoor, V.; Awasthi, K.; Jokar, E.; Diau, E. W.-G.; Ohta, N. Integral Method Analysis of Electroabsorption Spectra and Electrophotoluminescence Study of $(C_4H_9NH_3)_2PbI_4$ Organic−Inorganic Quantum Well. *J. Phys. Chem. C* **2018**, *122* (46), 26623−26634.
(33) Rana, S.; Awasthi, K.; Diau, E. W.-G.; Ohta, N. Interface- and Temperature-Sensitive Linear Electric Field Effects on Exciton Absorption of $CH_3NH_3PbI_3$ Perovskite Films. *J. Phys. Chem. C* **2023**, *127* (50), 24383−24392.
(34) Hamada, M.; Rana, S.; Jokar, E.; Awasthi, K.; Diau, E. W.-G.; Ohta, N. Temperature-Dependent Electroabsorption Spectra and Exciton Binding Energy in a Perovskite $CH_3NH_3PbI_3$ Nanocrystalline Film. *ACS Appl. Energy Mater.* **2020**, *3* (12), 11830−11840.
(35) Amerling, E.; Baniya, S.; Lafalce, E.; Zhang, C.; Vardeny, Z. V.; Whittaker-Brooks, L. Electroabsorption Spectroscopy Studies of $(C_4H_9NH_3)_2PbI_4$ Organic−Inorganic Hybrid Perovskite Multiple Quantum Wells. *J. Phys. Chem. Lett.* **2017**, *8* (18), 4557−4564.
(36) Ruf, F.; Magin, A.; Schultes, M.; Ahlswede, E.; Kalt, H.; Hetterich, M. Excitonic Nature of Optical Transitions in Electroabsorption Spectra of Perovskite Solar Cells. *Appl. Phys. Lett.* **2018**, *112* (8), No. 083902.
(37) Awasthi, K.; Kala, K.; Rana, S.; Diau, E. W.-G.; Ohta, N. Switching between Spectral Broadening and Narrowing of the Exciton Absorption Band of a $CH_3NH_3PbI_3$ Film on Altering the Polarity of an Applied Electric Field. *Appl. Phys. Lett.* **2020**, *116* (25), No. 251101.
(38) Ohta, N.; Okazaki, S.; Yamazaki, I. Stark Shift in Absorption Spectra of Langmuir-Blodgett Mixed Monolayer Films New Finding of a Complex Formation of Chromophoric Oxacyanine. *Chem. Phys. Lett.* **1994**, *229* (4−5), 394−400.
(39) Roiati, V.; Mosconi, E.; Listorti, A.; Colella, S.; Gigli, G.; De Angelis, F. Stark Effect in Perovskite/TiO_2 Solar Cells: Evidence of Local Interfacial Order. *Nano Lett.* **2014**, *14* (4), 2168−2174.
(40) Cappel, U. B.; Feldt, S. M.; Schöneboom, J.; Hagfeldt, A.; Boschloo, G. The Influence of Local Electric Fields on Photoinduced Absorption in Dye-Sensitized Solar Cells. *J. Am. Chem. Soc.* **2010**, *132* (26), 9096−9101.
(41) Ponomarev, I. V.; Deych, L. I.; Lisyansky, A. A. Electric-Field-Induced Narrowing of Exciton Linewidth. *Phys. Rev. B* **2005**, *72* (11), No. 115304.
(42) Yamada, Y.; Yamada, T.; Phuong, L. Q.; Maruyama, N.; Nishimura, H.; Wakamiya, A.; Murata, Y.; Kanemitsu, Y. Dynamic Optical Properties of $CH_3NH_3PbI_3$ Single Crystals As Revealed by One- and Two-Photon Excited Photoluminescence Measurements. *J. Am. Chem. Soc.* **2015**, *137* (33), 10456−10459.
(43) Sadegh, F.; Akin, S.; Moghadam, M.; Mirkhani, V.; Ruiz-Preciado, M. A.; Wang, Z.; Tavakoli, M. M.; Graetzel, M.; Hagfeldt, A.; Tress, W. Highly Efficient, Stable and Hysteresis−less Planar Perovskite Solar Cell Based on Chemical Bath Treated Zn_2SnO_4 Electron Transport Layer. *Nano Energy* **2020**, *75*, No. 105038.
(44) Zou, Z.; Qiu, H.; Shao, Z. Unveiling Heterogeneity of Hysteresis in Perovskite Thin Films. *Discovery Nano* **2024**, *19* (1), 48.
(45) Haidari, G. Three-Dimensional FDTD Optical Simulation of Surface Roughness in the Perovskite Solar Cell. *IEEE J. Photovolt.* **2019**, *9* (4), 1046−1050.
(46) Narra, S.; Jokar, E.; Pearce, O.; Lin, C.-Y.; Fathi, A.; Diau, E. W.-G. Femtosecond Transient Absorption Spectra and Dynamics of Carrier Relaxation of Tin Perovskites in the Absence and Presence of Additives. *J. Phys. Chem. Lett.* **2020**, *11* (14), 5699−5704.
(47) Ohta, N.; Awasthi, K.; Okoshi, K.; Manseki, K.; Miura, H.; Inoue, Y.; Nakamura, K.; Kono, H.; Diau, E. W.-G. Stark Spectroscopy of Absorption and Emission of Indoline Sensitizers: A Correlation with the Performance of Photovoltaic Cells. *J. Phys. Chem. C* **2016**, *120* (46), 26206−26216.

https://doi.org/10.1021/acs.jpcc.4c04645
J. Phys. Chem. C 2024, 128, 17134−17140